Insights into the electronic structure of Fe penta-coordinated complexes. Spectroscopic examination and electrochemical analysis for the oxygen reduction and oxygen evolution reactions

César Zúñiga Loyola, Gabriel Abarca, Soledad Ureta-Zañartu, Carolina Aliaga, Jose H Zagal, Moulay Tahar Sougrati, Frederic Jaouen, Walter Orellana, Federico Tasca

Insights into the Electronic Structure of Fe Penta-Coordinated Complexes. Spectroscopic Examination and Electrochemical Analysis for the Oxygen Reduction and Oxygen Evolution Reactions.

César Zúñiga Loyola[a], Gabriel Abarca[b], Soledad Ureta-Zañartu[a], Carolina Aliaga[a], Jose H. Zagal[a], Moulay Tahar Sougrati[c], Frédéric Jaouen[c], Walter Orellana[d], Federico Tasca[a]*

[a] Facultad de Química y Biología, Universidad de Santiago de Chile, Santiago, Chile.

[b] Universidad Bernardo OHiggins, Escuela de Obstetricia y Puericultura, Centro Integrativo de Biología y Química Aplicada (CIBQA), Santiago 8370993.

[c] ICGM, Univ. Montpellier, CNRS, ENSCM, Montpellier, France

[d] Departamento de Ciencias Físicas, Universidad Andrés Bello, Sazié 2212, 837-0136 Santiago, Chile.

*Corresponding author: Federico.tasca@usach.cl

Abstract

Fe phthalocyanine was coordinated to pyridine-modified carbon nanotubes and studied as a catalyst for the oxygen reduction (ORR) and oxygen evolution reactions (OER). X-ray Photoelectron Spectroscopy (XPS), Mössbauer, and Electron Paramagnetic Resonance spectroscopy (EPR) analysis supported that pyridine acts as an axial ligand to yield penta-coordinated catalytic active Fe sites. The impedance analyses show an increase in the double-layer capacitance (C_{dl}) value, corroborating the adsorption of the complexes to give FePc-Py-CNT. The evaluation of the electrocatalytic activity for the ORR was performed in both acid (0.1 M H_2SO_4) and basic (0.1 M KOH) media, while the evaluation of the OER activity was investigated only in alkaline medium. DFT studies revealed an increased length in the Fe-N binding of the pentacoordinate Fe-based site, leading to a decreased O_2-Fe binding energy, explaining the higher ORR and OER activity of FePc-Py-CNT relative to FePc-CNT.

1. Introduction.

With the ever-increasing demand for a less polluted atmosphere, the prices of platinum group metals (PGM) are rocketing due to the increasing demand for PGM-based catalysts[1,2]. Those catalysts are beneficial for the complete oxidation of hydrocarbons and the reduction of nitrogen oxides in the exhaust system of internal combustion engines, as well as in electrochemical devices where they facilitate key reactions for water electrolysers and fuel cells, namely the hydrogen and the oxygen evolution reactions (HER, OER) as well as the hydrogen oxidation reaction (HOR) and oxygen reduction reaction (ORR). In the reduction of oxygen, the breaking of the O-O bond is a process that requires a high dissociation energy (118 kcal mol^{-1})[3], while, in the OER the O-O bond formation is the rate-determining step[4]. The ORR can occur via indirect 2+2 or direct 4 electrons in both acidic and basic media, according to the following reactions:

In acidic media through 2+2 electrons the equation is:

$$O_2 + 2H^+ + 2e^- \rightarrow H_2O_2 \qquad E^0 = 0.682 \text{ V vs. SHE} \qquad (1)$$

$$H_2O_2 + 2H^+ + 2e^- \rightarrow H_2O \qquad E^0 = 1.77 \text{ V vs. SHE} \qquad (2)$$

In acidic media involving direct 4 electrons the equation is:

$$O_2 + 4H^+ + 4e^- \rightarrow 2H_2O \qquad E^0 = 1.23 \text{ vs. SHE} \qquad (3)$$

In basic media, a similar process occurs to produce HO_2^- through 2+2 electrons, and consecutively the reduction to it to OH^-:

$$O_2 + H_2O + 2e^- \rightarrow HO_2^- + OH^- \qquad E^0 = -0.076 \text{ V vs. SHE} \qquad (4)$$

$$HO_2^- + H_2O + 2e^- \rightarrow 3OH^- \qquad E^0 = 0.88 \text{ V vs. SHE} \qquad (5)$$

For the direct 4 electrons mechanism the corresponding equation to produce OH^- is:

$$O_2 + 2H_2O + 4e^- \rightarrow 4OH^- \qquad E^0 = 0.401 \text{ vs. SHE} \qquad (6)$$

In the case of oxygen evolution reaction (OER) in alkaline media, the $4e^-$ pathway proceeds according to the following equation:

$$4OH^- \rightarrow O_2 + 2H_2O + 4e^- \quad (7)$$

Also, OER involves multi-electron reactions where some elementary steps have an inverse correlation to the ORR, as in the following equation:

$$OH^- + * \rightarrow OH^* + e^- \quad (8a)$$

$$OH^* + OH^- \rightarrow O^* + 2H_2O + e^- \quad (8b)$$

$$O^* + OH^- \rightarrow OOH^* + e^- \quad (8c)$$

$$OOH^* + OH^- \rightarrow O_2 + H_2O + e^- \quad (8d)$$

*Where * represent an active surface site.*

For the ORR, the most active catalysts are based on Pt[5–8], while for the OER the state of art catalysts are based on Ir, and/or Ru, depending on the pH,[9,10] where the most active catalyst is IrO_2[11,12]. Pt was also initially studied for the OER by Rüetschi et al. in 1955[13].

Because of the scarcity and the cost of PGMs, numerous researches have been done to replace them with more abundant metals, such as Fe or Mn, to develop non-precious metal catalysts (NPMC). In 1964, Jasinski proposed a non-precious metal macrocyclic complex as a catalyst for the ORR[14]. Since then, major improvements in the design of M-N-C catalysts with single-metal-atom sites have been achieved, leaning on pyrolytic or non-pyrolytic approaches. In particular, Fe-based catalysts have proved to be equal or even more active for the ORR than the industrial standard Pt-based catalyst in alkaline environment[15–21]. For the OER phosphines, and metal oxides of Co, Ni, Mn, and Fe have been proposed[22–25]. Among the best NPMC for the ORR in alkaline medium, single-atom catalysts (SAC) such as metal-phthalocyanines and metal-porphyrins (i.e. macrocycles containing metal and four pyrrolic nitrogen atoms (MN4)) belong to the most promising ones. To further increase the activity towards the ORR and the stability of well-defined MN4 sites (in particular in acid medium), two main strategies have

been adopted: (*i*) the heat treatment of the catalyst[26–31]; (*ii*) the synthesis of complexes with more positive redox potential by the addition of electron-withdrawing residues[32,33]. Although pyrolysis of MN4 leads to progress in catalytic activity towards ORR,[34–38] this approach has several drawbacks, such as reduced control of the electronic and structural environment of the metal center, formation of multitudinous metal centers during pyrolysis, and limited site density due to the increased propensity of forming metal particles during pyrolysis with increased metal content[39,40].

In contrast, the exact coordination and ORR activity of MN4 macrocycles can be tuned by controlled synthetic approaches. For example, the introduction of electron-withdrawing groups to phthalocyanine ring has led to increased ORR activity[20,21,41] and clear electronic structure - activity correlations have been established for unpyrolyzed MN4 macrocycles, linking the formal redox potential of MN4 centers with the oxygen binding energy, and ORR activity, leading to well-known volcano plots[33,42,43]. Complexes with bio-inspired MN5 coordination from cytochrome c oxidase[44–46] have been developed to mimic the ORR active sites present in natural enzymes. The fifth nitrogen ligand, in axial position relative to the MN4 plane, can increase the redox potential and the stability of the metal center [18,47–53]. Similar strategies have also been adopted to enhance the activity of the catalyst towards the OER[54–56]. While it has been clearly demonstrated that FeN5 coordination is superior to FeN4 coordination for the ORR in alkaline medium, it is yet unclear if the same trend is valid for the OER in the same environment.

Also, insights into the ORR and the OER at FeN5 active sites are still missing. For instance, while it is clear that during the reductive elimination bear by d^8 and d^{10} complexes, a transition occurs from octahedral coordination geometry (M(IV)→M(II), M=Pd, Pt or M(III)→M(I), M= Rh, Ir) or from a square planar geometry to a linear/bent, it is not clear what happens with FeN5 complexes. To obtain insights into the electronic structure of Fe centres in FeN5 sites, we coordinated Fe phthalocyanine (FePc) to pyridine- (Py) modified CNT to obtain FePc-Py-CNT, and we studied the formed complex with ^{57}Fe Mössbauer spectroscopy, synchrotron X-ray photoelectron spectroscopy (XPS), electron paramagnetic

resonance (EPR), and DFT calculations. Along with this, catalytic performance for ORR (pH 1 and 13) and OER (pH 13) and electrochemical impedance spectroscopy (EIS) have been carried out to compare our results with bifunctional catalysts reported in the literature[57].

Finally, detailed spectroscopic studies of FePc-CNT (FeN4) and FePc-Py-CNT (FeN5) can be useful to better interpret the spectroscopic signatures of the Fe-based active sites in pyrolyzed catalysts[58,59].

2. Experimental.

2.1. Materials and methods.

Fe(II) phthalocyanine was obtained from Porphy Chem (Dijon, France), 4-Amino pyridine, and $NaNO_2$ were obtained from Sigma (St. Louis, USA). All aqueous solutions used Milli Q water (18.2 MΩ cm at 25ºC). Carbon nanotubes (CNT) were obtained from Cheaptubes inc (>90%)[50,60]. Dimethylformamide (DMF) and HCl were from Merck Inc. A typical three electrodes electrochemical cell was used to perform electrochemical measurements. Graphite bars were used as a counter electrode (supplied by Sigma-Aldrich) while an $Ag/AgCl_{sat}$ was used as a reference electrode. The potentials reported in this work are given against the reversible hydrogen electrode (RHE), and the change of scale from Ag/AgCl was done based on the Nernst equation[61,62]:

$$E\ vs.\ RHE = (E_{Ag/AgCl}) + (0.210\,V) + (0.059\,x\,pH) \qquad \text{(Eq. 1)}$$

A modified edge-plane pyrolytic graphite disk, 5 mm of diameter (area: 0.194 cm^2), was used as working electrode, with the exception of the EIS experiments, where a glassy carbon (GC) disc of 0.077 cm^2 was used. In some experiments, indicated in the text, a film of commercial Pt-Vulcan 20 wt.% using 10 µL of a 1 mg mL^{-1} to obtain a catalyst loading of 0.05 mg cm^{-2} was deposited on the surface of the edge-plane pyrolytic graphite or GC disks, which were used as working electrode (electrodes were from Pine

Instruments, Durham, NC, USA). In the experiments with rotating disc electrode a rotor system from PINE Instrument (Durham, NC, USA), was used.

Electrochemical processes were studied in 0.1 M KOH aqueous medium for alkaline (pH near 13) or 0.1 M H_2SO_4 (pH close to 1) for acidic medium. The electrochemical characterization and catalytic study were performed using an ultrapure N_2 and O_2 saturated atmosphere, at room temperature.

The determination of the number of electrons transferred during the ORR for each catalyst was done according to the Koutecky-Levich (K-L) equation[63] (Eq. 2), for which polarization curve at 5 mV s^{-1} were obtained at different rotation rates.

$$\frac{1}{j} = \frac{1}{j_k} + \frac{1}{0.6\ 20n\ FD^{2/3}\ \nu^{-1/6}\ C_{O_2}}\ \omega^{-1/2} \qquad \text{(Eq. 2)}$$

Where j_k: is the kinetic current density at a given potential (E); n: the number of transferred electrons; F: the Faraday constant (96.485 C mol^{-1}); D: the O_2 diffusion coefficient (1.9×10^{-5} cm^2 s^{-1})[64]; ν: the kinematic viscosity of the solution (0.01 cm^2 s^{-1})[65]; C_{O2}: the O_2 concentration (1.2×10^{-6} mol cm^{-3})[64]; and ω: the electrode rotation rate (rad s^{-1}).

In order to allow a better comparison among the electrodes, the rugosity factor F_R, was determined based on the capacitive current density, according to the methodology reported in a previous work [66,67]. (Briefly, $F_R = C_{dl}/C^{\circ}_{dl}$, considering C°_{dl} = 63.5 µF cm^{-2} the double-layer capacitance of a clean GC electrode (mirror polishing) and C_{dl} the double layer capacitance of the electrode determined by cyclic voltammetry at different potential scan rate in the potential region of the double layer. C_{dl} corresponds to the slope of a capacitive current density, j_C, versus the potential scan rate, v.

It is also high interest for fundamental interpretation of the electrochemical kinetics to quantify the number of active species. The active surface concentration (Γ, mol cm^{-2}) of FePc was determined by

cyclic voltammetry (CV), quantifying the electric charge associated with the redox couple Fe(III/II). In the CV experiments, for Langmuir monolayer adsorption, in the high overpotential region at 25°C, the current density *j* and the potential scan rate *v* are related by the equation[68].

$$j_p = \frac{q_1 F}{5.44\, RT}\, v \qquad \text{(Eq. 3)}$$

Where j_p, the peak current density is expressed in mA cm^{-2}, q_1 correspond to the electrical charge density associated to the active specie process (C cm^{-2}), *R*, *F* and *T* represent its usual meaning and *v*, the potential scan rate expressed in mV s^{-1}. 5.44 is a number that represent all the constant term considering the unities defined for Eq. 3. Thus, the parameter q_1 can be determined from the slope in a *j* against *v* plot, with linear correlation passing by the origin. From the q_1 value is determined the Γ parameters[63]

$$\Gamma = \frac{q_1}{nF} \qquad \text{(Eq. 4)}$$

For Pt based electrodes the surface concentration of Pt Γ_H values were determined by extrapolation of the double-layer charging current and integrating the charge for hydrogen desorption using 0.210 mC cm^{-2} as the specific charge for a monolayer of adsorbed hydrogen on Pt[69]

Synthesis of pyridine functionalized CNT. Sodium nitrite (5 g) was dissolved into distilled water (10 mL) and cooled to 0°C in an ice bath. 7 g of 4-amino pyridine (Py) were carefully dissolved in 5 mL of 4M HCl solution and added carefully to the sodium nitrite solution, letting rest 30 min on ice. The carbon nanotubes (CNT) (0.1 g) were then added to the nitrite amino pyridine mixture and left at 0 °C for three hours, after which the solution was left stirring overnight at room temperature. The functionalized CNT (CNT-Py) are obtained by filtration and washed repeatedly with Millipore water, drying at 80 °C overnight.

Formation of FePc-Py-CNT. A sample of the functionalized CNT-Py (100 mg) were dispersed in 50 mL of DMF in a 200 mL 3-necked round-bottomed flask through 15 minutes sonication. To this, FePc (50 mg) was then added with stirring and nitrogen gas bubbling. The mixtures were then connected to a condenser apparatus and refluxed at approx. 120 °C for three hours with constant N_2 flow. The resulting mixture was then filtered and repeatedly washed with Millipore water and dried overnight at 80 °C. After that, the ink preparation was carried out, dispersing 1 mg of the final mixture (FePc-Py-CNT) in 1 ml of 1:4 water-isopropanol (v/v ratio) to sonicate it for 30 minutes finally.

Formation of FePc-CNT. The FePc-CNT was obtained according to the previously reported protocol [21,49]. Briefly, CNT and FePc at 1:1 weight ratio was dispersed in 1:4 water-isopropanol (v/v ratio), then the dispersion was sonicated for 30 minutes. This ink was used to modify the electrode surface. Each ink (FePc-CNT and FePc-Py-CNT) was stored in a closed Eppendorf at room temperature, showing stability in this environmental condition after electrochemical studies.

Electrode preparation. The electrode was prepared by drop coating in two steps. First, 5 μL of the ink is drop cast on the electrode surface, and it was verified that it spread evenly before the operation is repeated once, resulting therefore in total of 10 μL of dispersion drop cast on the GC electrode. Finally, the ink was dried by a flux of ultrapure N_2.

Cyclic voltammetry (CV). Freshly prepared electrodes were characterized by CV in 0.1M KOH in order to determine its roughness factor and Fe(II)/Fe(III) surface concentration.

Electrochemical impedance spectroscopy (EIS). EIS measurements were carried out at constant potential in a one-compartment electrolytic cell with three-electrode configuration, in 0.1 M KOH electrolyte with a Luggin capillary for the reference electrode (inside a Luggin capillary closed with a Pt wire and filled with the supporting electrolyte) and a high area Pt helix or a carbon rode as counter electrode, using an

Autolab PGstat 128N equipped with FRA module. A 5 mV sinusoidal modulation in the 1 kHz-10 mHz frequency range, with 10 frequencies per decade. The impedance spectra analysis was performed with the NOVA 2.1 software, including the Kramers-Kronig transformation (KKt) analyses. The experiments take about 17 minutes, the temperature was controlled at the beginning and the end of the measurement, observing an increase of 1°C. The measurements were made in triplicate.

2.2. Ex situ physicochemical characterization

Mössbauer Spectroscopy analysis. The ^{57}Fe Mossbauer spectra were obtained at room temperature (295 K) using ^{57}Co: Rh source embedded in a rhodium matrix (^{57}Co (Rh)). Triangular velocity waveform and a gas-filled proportional counter were used in order to detect the γ rays. Isomer shift was determined relative to α-Fe (20 μm, at 295 K). Samples were prepared by pressing ca. 100 mg of powder inside a pill shape (2 mm thick and 15 mm of diameter). The spectra were fitted with an appropriate combination of Lorentzian profiles representing quadrupole doublets and magnetic sextets by the least-squares methods using the program PC-Mos II[70].

X-Ray photoelectron spectroscopy (XPS). XPS measurements were carried out at the LNLS (Brazilian Synchrotron Light Laboratory) at the SXS beamline end-station. The spectra were collected using an InSb (111) double crystal monochromator at a fixed photon energy of 1840 eV. The O_2 treatment at room temperature (RT) was accomplished in the preparation chamber using a pressure of 20 psi of 5% O_2 + 95% He during 1 h.[71] The sample was investigated using the survey scan, as well a with narrow scans in the Fe 2p, O 1s, and C 1s regions. The hemispherical electron analyser (PHOIBOS HSA500 150 R6) was used and set at a pass energy of 20 eV, and the energy step was 0.1 eV, with an acquisition time of 100 ms/point. The overall resolution was around 0.3 eV. The base pressure used inside the chamber was around 5.0×10^{-9} mbar. The monochromator photon energy calibration was done at the Si K edge (1839 eV). The peaks were adjusted with an asymmetric Gaussian-Lorentzian sum function (30 % Lorentzian

contribution). Also, all peaks were adjusted using a Shirley-type background. In the fitting procedure, the full width and half maximum (FWHM) value was kept constant over the adjustment procedure. The fitting at the Fe 2p electronic level was performed considering the well-known satellite peaks due to the shakeup effect associated with Fe.[72]

Electron paramagnetic resonance spectroscopy analysis (EPR). EPR measurements were carried out for four different powder samples (a) FePc-Py-CNT, (b) FePc-CNT, (c) Py-CNT, and (d) CNT. The spectra were obtained with Bruker EMX-1572 spectrometer at 298K, working at 9.39 GHz (X-band).

2.3. Computational analysis.

Spin-polarized density functional theory (DFT) calculations were performed with the Vienna ab-initio simulation package (VASP) [73] with a similar set-up as reported by Cao *et al*[18]. The semi-local exchange-correlation functional in the Perdew-Burke-Ernzerhof form was used[74], including dispersion corrections for the van der Waals interaction, as proposed by Grimme (DFT-D2)[75]. A plane wave cut-off energy of 400 eV and the projector augmented-wave method for the core-valence interaction were employed[76]. A metallic single-walled carbon nanotube with (8,8) chiral indices, 11 nm in diameter and 288 total atoms, was simulated with a large supercell with periodic boundary conditions along the CNT axis. We consider a vacuum region of 20 Å to ensure negligible interaction between CNT lateral images. Due to the large size of the supercell, only the point for the Brillouin-zone sampling was considered.

3. Results and Discussion.

3.1. Physicochemical characterization.

EPR Analysis measurements. The EPR spectrum was determined for FePc-Py-CNT and FePc-CNT samples (Figure 1a). The g-factors determined from the spectra are g_{iso}: 2.032 and 2.072 for FePc- CNT and FePc-Py-CNT, respectively, where the EPR signal are related to the odd spin of Fe(III) centres in

FePc exposed to O_2, while Fe(II) centres would be EPR silent. The increase in g-factor for Fe(III) centres in FePc-Py-CNT vs. FePc-CNT could be associated with the possible electron withdrawing character of the Py axial ligand[18]. Similar increase in g-factor has been observed due to the presence of halogen groups in the periphery of the phthalocyanine ring[21]. A high spin delocalization in CNT could also be responsible for the high value of g_{iso} (i.e. g_{iso}: 2.072)[77]. The EPR spectra of Py-CNT and CNT were also recorded and are shown in the supporting information file (Figure S1) and the g-factors are g_{iso}: 2.083 and 2.194, respectively. For these samples, the EPR signal is specifically associated with surface defects[78,79]. According to these EPR data, the presence of Py axial ligand in FePc-Py-CNT and its electron pulling character are corroborated[21,80].

^{57}Fe Mössbauer Spectroscopy This technique can give information about the spin state and oxidation state of the Fe metal centre. In Fig. 1 (b) the ^{57}Fe Mössbauer spectrum is presented for FePc-Py-CNT catalyst. The spectrum shows three deconvoluted spectral components whose fitted isomeric shift (δ_{iso}), quadrupole splitting (ΔE_Q), and the full width at half maximum (FWHM) values are summarized in Table S1. First, it is clear that none of the three doublets can be assigned to the β-Fe(II)Pc, which has a distinct ΔE_Q value of 2.6 mm s^{-1} [81,82], much higher than observed for any of the three fitted doublets with ΔE_Q values ranging from 0.39 up to 1.04 mm s^{-1} (Table S1). Also, none of the three doublets can be assigned to Fe(II)Pc coordinated with two axial Py ligands, for which ΔE_Q is also high, at 1.94 mm·s^{-1}.[81] In contrast, the doublet D_b[82] has spectral parameters (δ_{iso} 0.22 mm s^{-1}, ΔE_Q 1.04 mm s^{-1}) that are similar to those reported for a FePc monolayer supported on Vulcan carbon black (δ_{iso} 0.37 mm s^{-1}, ΔE_Q 0.91 mm s^{-1}, reported in ref. [82,83] for the sample prepared via vacuum evaporation of FePc and deposition on carbon, without any annealing). The component D_b might therefore be assigned to FePc molecules adsorbed on CNT, at locations where the surface was free of Py groups.

The lack of previous ^{57}Fe Mössbauer studies on well-defined FePc molecules axially grafted to carbon surfaces prevents a straightforward assignment of the other two spectral components, D_a and D_c. Their lower δ_{iso} and ΔE_Q values with respect to that for FePc is in general agreement with the trends reported for porphyrins with axial Py ligand relative to the same porphyrins without axial Py ligand.[84] For example, a decrease in ΔE_Q from 1.95 to 0.67 mm/s was reported after addition of a Py axial ligand to Fe-octaethylporphyrin.[84] A recent study from Cheng *et. al.* reported the axial ligation of FePc by N-groups from a N-doped carbon support.[85] The ^{57}Fe Mössbauer spectrum of that catalyst showed two doublets, the first one with (δ_{iso}, ΔE_Q) of (0.45, 0.63 mm/s). That doublet has Mössbauer parameters similar to doublet D_c in the present work (δ_{iso} and ΔE_Q of 0.39 and 0.54 mm/s, respectively, Table S1), and was assigned to an X-Fe(III)N_4–Y octahedral coordination, with X, Y being axial ligands such as O or N. We therefore tentatively assign D_c in the present work to O-Fe(III)N_4-N coordination, where N is from Py and O from adsorbed O_2. The presence of adsorbed O_2 on top of ORR-active Fe centres is expected when Mössbauer spectra are acquired in ambient air. This assignment is also supported by a study on oxygenated FePc crystals. Kuzmann et al.[86] showed that β-FePc crystals can adsorb O_2 at near ambient temperature, and that this process modified the Mössbauer spectra with a strong decrease in the intensity of the doublet specific for β-Fe(II)Pc and the appearance of four new doublets, assigned to the adsorption of one or two O_2 molecules per FeN_4 centre, forming μ-peroxo or μ-oxo bridges between stacked FePc molecules.[86] Two new doublets had similar δ_{iso} of *ca* 0.4 mm/s at RT but different ΔE_Q values (0.59 and 0.96 mm/s, for sample C in that work) while two other doublets had also similar δ_{iso} of ca 0.12 mm/s at RT but again different ΔE_Q values (0.46 and 0.84 mm/s, for sample C in that work). These four doublet components were described as being consistent with an Fe(III) high-spin configuration, in this case an O-Fe(III)N_4-O octahedral coordination. In particular, the Mössbauer parameters of species III in Ref. [86] match well those of D_c in the present work, while the low δ_{iso} and low ΔE_Q values of species V match well those for D_a. Based on these earlier works on FePc covalently attached to CNT or oxygenated FePc crystals, we

tentatively assign both doublets D_a and D_c to octahedral O-Fe(III)Pc-N coordination, with O from adsorbed O_2, and the fifth N ligand coming from Py as a second axial ligand. However, one must keep in mind that the fitted δ_{iso} and ΔE_Q values of doublet D_a and/or D_c could also correspond to an iron centre in +II oxidation state and in low spin state. The existence of Fe(II)Pc state in ambient air with the present FePc-Py-CNT sample might be possible if some Fe centres are not accessible by air, e.g. via the stacking of two FePc molecules such as in β-FePc crystals, with one FePc being attached to CNT via a Py axial ligand (N-Fe(II)Pc-N coordination). Anyway, the presence of Fe(II) in the low spin state is not observed in XPS analysis (see below).

X-Ray Photoelectron spectroscopy (XPS). High resolution XPS analysis for FePc-CNT and FePc-Py-CNT before exposure to O_2 (Fig. 2 (a) and (b)), show a spin-orbit doublet of Fe $2p_{3/2}$ at 708.5 eV and 708.7 eV, respectively. The broad Fe $2p_{3/2}$ peak indicates the presence of Fe in different valence states according to the values summarized in Table S2. The differences in binding energies detected for Fe $2p_{3/2}$ peak is related to the alterations in the electronic structure, where the Fe centre can perform a rearrangement of the D_{4h} local symmetry (Fe surrounded by four-coordinated nitrogen ligands) through a non-planar configuration supported by XPS Fe 2p core level signal[18]. Because of the presence of a site with five coordinated nitrogen, the Py can modulate the electronic environment of Fe^{2+}/Fe^{3} showing a shift towards high-binding energy values[50].

The Fe^{2+}/Fe^{3+} ratio, for FePc-CNT and FePc-Py-CNT before exposure to O_2, was determined by iron contribution summarized in Table S3, and S4. The contribution is related to the formal potential of the catalyst which is associated to the catalytic performance[21,87]. The XPS Fe 2p core level spectra show the peak position at 708.5 eV for the FePc-CNT composite (Figure 2 (a)). On the other hand, the Fe $2p_{3/2}$ core level spectra in FePc-Py-CNT is upshifted to 708.7 eV (Fig. 2 (b)). In this sense, the energy shift of 0.2 eV can be consider significant. Similar to what we reported before[71] after O_2 treatment, there is no

significant energy shift for Fe $2p_{3/2}$ core level spectrum, indicating that no stable Fe−O_2 adducts are formed in the gas phase. These results are expected since these molecules are ORR catalysts, not O_2 carriers, and they should not bind O_2 too strongly. In the mentioned case[71], we reported a Fe $2p_{3/2}$ shift after O_2 exposure between 0.1 to 0.3 eV. Then, as Fe atom is coordinated with the Py group at the axial position in FePc–Py–CNT, the extra ligand leads to the change of electron density on Fe, indicating a higher oxidation state of the Fe than in the FePc–CNT. These results are in agreement with the values of the formal potentials observed (Table 1)[88]. Moreover, the presence of the pyridinium ligand has a strong impact on the core ionization energies of Fe (Fe 2p photoelectron peaks), associated with the ligand-to metal charge transfer process. The corresponding binding energies behaviour could be understood from back-bonding between Fe metal centre with strong sigma donation, from lonely nitrogen electron pairs of pyridine to half-filled d_z^2 orbital, and consecutively metal-to-ligand charge transfer via weak π orbital to π* unoccupied orbital in Py axial ligand, leading to a Fe^{3+} character of the metallic centre[89–91]. In Figure 2 (c), and (d) are shown the XPS spectra for Fe $2p_{3/2}$ in FePc-CNT and FePc-Py-CNT after exposure to O_2, where it is possible to observe an increasing Fe^{2+}/Fe^{3+} ratio for both samples (Table S2). As expected, a significant energy shift for the Fe $2p_{3/2}$ core level spectrum of FePc-Py-CNT was observed, suggesting that stable Fe-O_2 adducts are formed during the O_2 exposure. Indeed, after O_2 exposure, an initial ratio of 0.33 was raised to 0.57 for FePc-Py-CNT (as for the Fe^{2+}/Fe^{3+} ratio). Therefore, an effective rearrangement of the d_z^2 orbital, due to a change of local symmetry form of the five-coordination system to a hexacoordinate one, is observed for FePc-Py-CNT.

On the other hand, a Fe^0 contribution was included in Table S4 for the surface of the FePc-Py-CNT catalyst, only after the exposure to O_2, because in the fitting procedure, the FWHM value was kept constant over the adjustment procedure. The fitting at the Fe 2p electronic level was performed considering the well-known satellite peaks due to the shakeup effect associated with Fe. Based on these considerations, we observed for FePc-Py-CNT after O_2 exposure an increase of Fe^{2+}/Fe^{3+} showing a shift

towards high-binding energy values. These results suggest that the Py can modulate the electronic environment of the Fe center, indicating a "metallic character" after O_2 treatment for the Fe center.

3.2. Oxygen reduction reaction (ORR).

Cyclic voltammetry at 100 mV s^{-1} for FePc-CNT and FePc-Py-CNT modified electrodes in deaerated acidic and basic media are shown in Figure 3, black solid line. As can be observed, a well-defined faradic process appears for two reversible formal potentials Fe(II)/(I) and Fe(III)/(II) at more negative and positive values, respectively, according to literaturere[41,50,92], where the focused process is the last one (see grey circles). The surface concentration (Γ) was obtained from cyclic voltammetry at different scan rates and considering the geometric electrode area (0.194 cm^{-2}), according to Eq. (3) and (4). The Γ values are summarised in Table 1. The values range between 10^{-9} to 10^{-10} mol cm^{-2}, in agreement with the previous results reported for modified CNT [41,87,93]. The formal potential (E^0') of Fe(III/II) couple in FePc-CNT modified electrode are 0.657 and 0.801 V vs. RHE in acid and basic media, respectively, where the formal potential shifts to negative values in acidic media is associated with nitrogen protonation, similar to what happens with pyrolyzed catalysts[94] . Meanwhile for FePc-Py-CNT, the Fe(III/II) redox couple appears at 0.699 and 0.871 V vs. RHE in pH 1 and 13, respectively (Table 1). The formal potential Fe(III/II) redox couple is positively shifted by 42 mV in acid and 70 mV in basic electrolyte with respect to FePc-CNT, evidencing that the presence of pyridine in FePc-Py-CNT has an electron withdrawing effect as axial ligand, analogous to peripheral electron-withdrawing groups in phthalocyanines[33,87]. This is also supported with the changes observed in the Mossbauer and XPS spectra. This phenomenon, that has also been reported in previous works[18,50], would act favouring a higher oxidation iron state due to inductive effect, which decreases the *d* electron density at the iron central metal[95].

Linear scan voltammetry (LSV) was performed at 5 mV s^{-1} in a saturated O_2 atmosphere (red curve in Fig. 3, using FePc-CNT and FePc-Py-CNT modified electrodes in alkaline and acidic medium). Also, a

graphite electrode modified with a film of Pt/C 20 wt% catalyst has been tested under the same experimental conditions in both media for comparison (grey dashed line in Fig. 3). In alkaline media (Figure 3 (a) and (b)), the current density for the Pt/C 20% catalysts is lower than the theoretical value of -6.0 $mAcm^{-2}$. This is in accordance with values reported in the literature[96,97], where the interference of an outer-sphere mechanism at pHs lower than 10 is considered as a consequence of the OH^- ions adsorbed at the electrocatalytic surface[98,99]. In Figure 3 (b) we can observe that with FePc-Py-CNT at pH 13 the onset potential for the ORR is shifted to a more positive value than platinum based catalyst. In contrast, in Fig. 3 (d), an increase in the overpotential for the ORR is observed at pH 1, if compared to the Pt catalyst, being this difference close to 110 mV. We must emphasize that the best catalytic performance was obtained in basic solution. In fact, FePc-Py-CNT at pH 13 (Figure 3 (b)) exhibits ΔE_{onset} of 38 mV and $\Delta E_{1/2}$ of 85 mV less negative than Pt/C 20 wt% commercial catalyst. This fact corroborates the notable influence of axial Py coordination, indicating a more efficient electronic configuration of the metal centre for the ORR. It is possible to associate the increment in the catalytic activity at pH 13 with a shift to more positive values of the formal potential of Fe (III)/(II). This correlation has been proved also for some pyrolyzed NPMC catalysts.[34,100]

The number of the electrons transferred has been estimated by the K-L equation (2) (Inset Fig. 3 (a-d)). The results evidence that using FePc-CNT modified electrode, 2.6 electrons are transferred in acid media, indicating that O_2 is reduced preferably by a 2 e^- mechanism yielding mostly H_2O_2. The presence of the Py axial ligand improves the catalytic process, and O_2 is almost completely reduced to H_2O with a transfer of 3.6 e^-. Both FePc-CNT and FePc-Py-CNT perform very well in basic media and 3.8 and 4.0 e^- are transferred, respectively, reducing molecular oxygen to OH^-, mainly. The Tafel slopes were determined according Butler-Volmer equation[63] from each polarization curves at 1600 rpm, with limiting current density correction[63,101]. Tafel slopes are summarized in Table 1. At pH 1, values of -0.086 and -

0.097 V dec^{-1} were obtained for FePc-CNT and FePc-Py-CNT, respectively, suggesting that two parallel mechanisms are participating for ORR with different rate-determining step[33,50,98].

In comparison, for basic media, FePc-CNT shows a Tafel slope of -0.044 V dec^{-1}, indicating that the rate-determining step is the second-electron transfer which is preceded by a fast oxygen adsorption chemical step, and the fast first one-electron transfer step,[87,102,103] similar to Pt/C 20 wt% catalyst used to compare our measurement in both pH values. FePc-Py-CNT at pH 13 shows the lowest Tafel value, close to -0.022 V dec^{-1}, which is related to O_2^- protonation as a rate-determining step influenced by Py axial coordination [18,104]. All the electrochemical parameters are summarized in Table 1.

Table 1. Elec

Electrochemical parameter for FePc-CNT, Fe-Py-CNT and Pt/C 20 wt% in acid and basic media.

Complex	Media	$E^{0'}_{Fe(III)/(II)}$ V vs RHE	E_{onset}(*) V vs RE RHE	Tafel (V dec^{-1})	n° e^- (K-L)	Γ mol cm^{-2}	TOF@ (0.80 V vs. RHE) s^{-1}
FePc-Py-CNT	0.1 M NaOH	0.871 ± 0.002	1.017 ± 0.001	-0.022 ± 0.001	4.0 ± 0.03	$8.29x10^{-10} \pm 1x10^{-11}$	1.78
FePc-CNT	0.1 M NaOH	0.801 ± 0.003	0.916 ± 0.001	-0.044 ± 0.002	3.8 ± 0.10	$7.94x10^{-10} \pm 1x10^{-11}$	1.01
FePc-Py-CNT	0.1 M H_2SO_4	0.699 ± 0.003	0.844 ± 0.002	-0.097 ± 0.003	3.6 ± 0.02	$3.94x10^{-9} \pm 2x10^{-10}$	0.02
FePc-CNT	0.1 M H_2SO_4	0.657 ± 0.003	0.784 ± 0.001	-0.086 ± 0.001	2.6 ± 0.07	$1.62x10^{-8} \pm 1x10^{-10}$	-
Pt 20% Vulcan	0.1 M NaOH	-	0.979 ± 0.001	-0.046 ± 0.001	4.0 ± 0.03	$1.18x10^{-9} \pm 1x10^{-10}$	0.85
Pt 20% Vulcan	0.1 M H_2SO_4	-	0.954 ± 0.001	-0.047 ± 0.001	4.0 ± 0.03	$2.8310^{-10} \pm 2x10^{-11}$	3.82

(*) The Onset potential (E_{onset}) was evaluated at 0.1mA cm^{-2}

The turnover frequency values (TOF) (Table 1) were calculated at 0.8 V vs. RHE from the O_2 reduction polarization curve and the respective electrode coverage (Γ), (Eq. 4)[21] for the various electrodes.

The obtained TOF value for Pt/C 20% in alkaline media is lower than in acid media (0.85 and 3.85 respectively) because the surface concentration of the active sites (Γ, mol cm^{-2}) in acid is lower than in

basic media according to Table 1 and the TOF value is inversely proportional to the surface concentration of the active sites. In alkali, the TOF values range from 1.708 to 1.01, where the Py axial ligand in alkaline media allows for TOF numbers higher than the TOF value of Pt/C 20% (0.85 at 0.8 V vs. RHE). Indeed, the low electron density on the Fe metal centre when in the presence of the axial coordination is strongly evidenced in acidic media, where the TOF value was one order magnitude higher for FePc-Py-CNT (0.02) concerning FePc-CNT (0.00).

3.3. Oxygen evolution reaction (OER).

The bifunctionality of redox catalysts for the ORR and the OER are very important because of the possibility to use those catalysts in metal-air batteries. The bifunctionality of FePc-Py-CNT has been tested in an N_2 saturated atmosphere for the OER using 0.1 M KOH solutions and polarization curves at 5 mV s^{-1}. For those studies, a crucial parameter is the potential difference (ΔE) at which the ORR and the OER are performed, according to the following equation:[105]

$$\Delta E = [E_{j_{10}} OER] - [E_{1/2} ORR] \qquad \text{(Eq. 5)}$$

Where Ej_{10} is the potential for the OER when the current achieves a value of 10 mA cm^{-2} and $E_{1/2}$ is the half-wave potential for the ORR polarization curve.

The ΔE parameter allows us to compare the performance with several kinds of catalysts reported in the literature. Figure 4 (a) shows both polarization curves for ORR (blue line) and OER (red line) with ΔE value of 0.680 V for FePc-Py-CNT, which can be compared with the values reported in the literature for precious metals group (PMG) and summarized in Table S5. Furthermore, high bifunctional performance for FePc-Py-CNT has been observed even when it is compared to pyrolyzed catalysts, suggesting that pyridine axial coordination in FePc catalyst could be proposed as a convenient approach to develop bifunctional catalysts. The Tafel slope for OER on FePc-Py-CNT was 0.214 V dec^{-1} (Fig. 4 (b)), which

well agrees with reported values for the OER[105–108]. According to this value, a four-electron pathway is probably involved during the OER to produce O_2 in alkaline media, favouring the catalytic process according to the reaction (7) [55,109–111], where the active site is the Fe metal, with a predominant presence of Fe^{3+} species, to perform the direct oxidation of adsorbed OH^- species[112,113]. A range of Tafel values reported in the literature goes from 650 to 50 mV dec^{-1} [105,114,115] suggesting different OER mechanisms[108].

$$4OH^- \rightarrow O_2 + 2H_2O + 4e^- \quad (7)$$

3.4. Electrochemical impedance spectroscopy (EIS).

As pointed out in the Experimental Section the EIS data were obtained using a GC disc electrode because the experiments showed better reproducibility, probably due to a better current distribution. It is known that with too rough electrodes it is difficult to obtain good impedance measurements. Three working electrodes were used in order to separate the contributions of each component to the global process. This implies that the EIS data were obtained for (a) CNT/GC, (b) Py-CNT/GC, and (c) FePc-Py-CNT/GC electrodes, in 0.1 M KOH. The freshly prepared electrodes were stabilized by 10 CVs at 0.02 V s^{-1} in deaerated 0.1 M KOH. An example of the stabilized CV is plotted in Figure S2 for each kind of GC modified electrode, where is evidenced a large difference in the capacitance between the different electrodes (double layer region in the CV in Figure S2), fact that should be corroborated with the EIS measures. Roughness factor (F_R) were obtained for all electrodes (see Tables S6 for the respective values). As was expected, independent of the support electrode, the CV with FePc-Py-CNT/GC electrode (Fig. S2, blue line) shows the same two couples of peak current associated to de Fe(II/I) and Fe(III/II) processes. In consequence, the coating by Fe-based species (Γ_{Fe}) were determined in the same way as described before, using the Eqs. (3) and (4). At higher applied potential than peak 2a, the OER is starting.

In O_2 saturated electrolyte, the CV shows the characteristic peak associated to the ORR (Figure S3), which occurs with lower overvoltage using FePc-Py-CNT/GC electrode and it is inhibited at Py-CNT/GC surface. In consequence, in principle impedance experiments for ORR were developed at two constant potentials, 0.89 and 0.79 V vs. RHE in deaerated and oxygen saturated solution. In Fig. S4 are shown as example the Nyquist plots obtained for FePc-Py-CNT/GC electrode. As can be seen, the curves are complex, and do not follow a unique equivalent circuit pattern during the process. No notable differences are observed in the Nyquist plots of the electrodes modified with FePc-Py-CNT/GC at these two potentials. In view, for the ORR (open symbols in Fig. S4) a typical Randles, $R_u(R_FC_{dl})$ circuit was used to determine the characteristic parameters, using the Fit and Simulation tool of Nova 2.2 software, considering valid the results with error lesser than 10%. R_u represent the non-compensated resistances, that at least include the solution resistance R_s and any other resistance to charge transport that may be generated by the film deposited on the electrode surface. R_F correspond to the faradaic resistance associated to the electrochemical reaction and C_{dl} would be associated to the charge of the double layer. In deaerated solution (closed symbol in Fig. S4), purely capacitive behaviour, a R_uC_{dl} equivalent circuit was used to fit. The results are given in Table S6.

Figure 5 (a) shows in a comparative way the impedance results for the 3 types of electrodes studied in O_2 saturated 0.1 M KOH, such as Nyquist and Bode diagrams at 0.88 V. This Figure clearly shows that CNT/GC and FePc-Py-CNT/GC electrodes behave very similar at low frequencies (Bode plots, a 2 and 3), whereas the electrode modified with Py-CNT/GC show the worst system for the electron transfer process since the charge transfer resistance is very high. See the values in Table S6. The Nyquist plot is more sensible a low frequencies, evidencing the possibility of a diffusion control using the FePc-Py-CNT/GC.

Respect to Table S6, there are an increase in the double layer capacitance at 0.88 V vs. RHE for ORR process using CNT/GC and FePc-Py-CNT/GC electrodes, which could be attributed to adsorption of

reagents or intermediates of the reduction process favoured by Py, which blocks the reaction if the overpotential is increased by 0.1 V (E = 0.79 V vs. RHE). The system behaves as a capacitor at low frequencies. The Py-CNT/GC electrode shows a Phase angle that tends to -90°. Whereas for CNT/GC and FePc-Py-CNT/GC electrodes, the maximum value for phase angle is very similar, close to -68.8°, far of -45° expected for FePc-Py-CNT/GC electrode for a diffusion-controlled process, showing a complex electrochemical process.

EIS measurements were also carried out for the OER. In order to determine de potential region of interest, CVs increasing the positive limit were obtained at 20 mV s^{-1} in deaerated 0.1 M KOH using FePc-Py-CNT/GC electrode (Fig. S5). This Figure reflects for one side the stability of the electrode at higher applied potential and by the other, the effective increase in current density at not so high potential. The stability of these electrodes was determined evaluating the electrical charge Q, against potential, *E*, for repetitive potential cycles and after the EIS experiments. The plot shows a practically closed oval, evidencing the excellent reversibility of the process (not shown). In consequence, Nyquist plot at five potential values, between 0.78 and 1.43 V, were obtained in deaerated 0.1M KOH using FePc-Py-CNT/GC electrode (Fig. S6). As was expected the Faraday resistance decreases with the potential increases. The values are given in Table S7. Note that when the electrode surface is at 0.78 V vs. RHE Fe in FePc-Py-CNT is as Fe(II), and at 1.18 V vs. RHE and higher, Fe atoms are as Fe(III), and 1.38 V vs. RHE potential is close to the $E_{onset,}$.

Call the attention that the R_u, the uncompensated resistance that is an intrinsic characteristic of the electrolyte and electrode material are near one tenth of those observed for ORR, which is probably a consequence of the reactive species being OH^-, which must already be adsorbed at a much less positive potential. This agrees with the increase in double layer capacity near 10 times. However, the R_u values are

higher at potentials where the OER reaction occurs, in agreement with an increase in the resistance to ionic transport by the film.

Returning to Fig.5, in order to separate the different contributions to the impedance measurements for the OER, in Fig. 5 (b-1) are plotted the Nyquist plot for electrodes modified with CNT/GC, Py-CNT/GC, and FePc-Py-CNT/GC at 1.38 V. Again, Py-CNT/GC electrode appears highly resistive, whereas FePc-Py-CNT/GC electrode is somewhat less resistive than electrode CNT/GC (see the inset in Fig.5b1). The impedance fitted parameters are tabulated in Table S8.

According to Table S8, variation in the values for the uncompensated resistance R_u with the components of the electrode agree with our previous supposition that this term does not only correspond to the resistance of the solution but also has a factor dependent on the ionic conductivity (mass transport) of the film deposited on the electrode surface. The R_u is more significant for Py-CNT/GC, despite it having the lowest roughness. The FePc-Py-CNT/GC shows the higher double layer capacity, evidencing a better disposition to adsorb the reaction components, similar to previously observed for ORR in Table S6. Therefore, FePc-Py-CNT/GC exposes higher active site compare Py-CNT/GC and CNT/GC, respectively[116], in total agreement with the explanations given in the first part of the experimental results of this work.

In conclusion, the impedance study, well agrees with a bifunctional behaviour in the FePc-Py-CNT/GC electrodes due to the fundamental role of the Fe(III) in the FePc-Py structure, the electrode activity increases by the increases in the OH^- adsorption promoted by CNT.

3.5. Computational analysis.

DFT calculations were performed for FePc interacting with a single-walled CNT of 1.1 Å in diameter through physisorption (FePc-CNT), and chemisorption by an axially-coordinated pyridine (FePc-Py-

CNT). Graphene was used to estimate the effect of the CNT curvature because experiments were performed with a larger CNT of 2 Å in diameter.

Figure 6 shows the FePc-CNT structure in the equilibrium geometry. We find that FePc is strongly attached on the CNT with binding energy of 1.692 eV, preserving its magnetic moment after adsorption (m=1.98 μ_B). The shortest distance between the CNT surface and the FePc molecule is found of 2.95 Å. For the case of FePc on graphene (FePc-G), the FePc binding energy is even larger, -2.323 eV, and the distance between the graphene plane and FePc is found of 3.526 Å. Here, the FePc magnetic moment is also preserved (m=2.00 μ_B). Therefore, we can conclude that the FePc curvature, as induced by the interaction with the CNT, slightly alters its spin state. Table 2 shows results for the total energies of FePc physisorbed on the CNT and graphene for the allowed spin states, before and after the O_2 adsorption. The four Fe-N bond distances are almost the same (1.93 Å), indicating the coordination Fe-N4 remained centrosymmetric. Once O_2 is adsorbed on the Fe centre in the most stable end-on configuration, the magnetic moment changes to m=0 μ_B, suggesting an antiparallel coupling with the O_2 molecule. However, the m=2 μ_B spin state is very close in energy, about 0.03 eV higher, which indicates that both spin states are equally probable. After the O_2 adsorption, the Fe atom moves out of the macrocycle plane about 0.2 Å, while two Fe-N bond distances increase, showing an asymmetric relaxation (1.93 and 1.95 Å, see Table S9). Also, the O-O bond distance increases by about 3.6% relative to the free O_2 molecule. The O_2 binding energy is calculated to be of -0.809 eV.

Table 2. Total energy of the FePc-CNT and FePc-G with and without adsorbed O_2 for the allowed spin states. E_0 is the lowest energy state.

m (μ_B)	**FePc-CNT**	**FePc-G**	**O_2-FePc-CNT**	**O_2-FePc-G**
	***E*total (eV)**	***E*total (eV)**	***E*total (eV)**	***E*total (eV)**
0	E_0 + 0.267	E_0 + 0.256	E_0	E_0
2	E_0	E_0	E_0 + 0.032	E_0 + 0.032
4	E_0 + 0.183	E_0 + 0.231	E_0 + 0.164	E_0 + 0.162

Figure 7 shows the equilibrium geometries of FePc-Py-CNT before and after the O_2 adsorption. The FePc macrocycle also preserves its magnetic moment in the most stable state (m=2 μ_B). However, the spin states m=1 and 3 μ_B are close in energy, 0.04 and 0.03 eV higher, respectively. Therefore, three different spin configurations are equally probable. The four Fe-N bond distances are almost the same (1.94 Å), showing a symmetric configuration. After the O_2 on the Fe centre in the end-on configuration, the most stable spin state has a magnetic moment m=1 μ_B, follow closely by the spin states m=0 and 2 μ_B, with a difference in energy of 0.03 eV. Therefore, the O_2-FePc-Py-CNT system (Fig. 7, and Table 3) might be found in different spin configurations (m=0, 1, 2 μ_B). Similarly, to the O_2-FePc-CNT system, the Fe atom moves out of the macrocycle plane about 0.2 after the O_2 adsorption, while two Fe-N bond distances increase, showing an asymmetric relaxation (1.94 and 1.96 Å, see Table S10). Also, the O-O bond distance increased about 4.1% with respect to the free O_2 molecule. The O_2 binding energy is calculated to be -0.758 eV. Comparing with O_2-FePc-CNT, in the O_2-FePc-Py-CNT system the Fe-O_2 adduct is 0.051 eV less strong, while the O-O bond distance is slightly longer, suggesting better ORR catalytic activity for O_2-FePc-Py-CNT.

Neya reported [117] that a more contracted coordination hole of Fe-N4 complexes generates an increase in energy splitting between $d_{x^2-y^2}$ and d_{z^2} where the last one orbital (d_{z^2}) is stabilized, favouring the Fe-O_2 binding strength. In this sense, we suggest that Py axial ligand in FePc-Py-CNT could slightly increase the d_{z^2} (due to more distance between N and Fe atoms, or a more expanded coordination hole of MN4) energy orbital in contrast to FePc-CNT, consecutively Fe(II)-O_2 interaction is less intense, in agreement with theoretical studies.

Table 3. Total energy of the FePc-Py-CNT and FePc-Py-G with and without adsorbed O_2 for the allowed spin states. E_0 is the lowest energy state.

m (μ_B)	FePc-Py-CNT	FePc-Py-G	O_2-FePc-Py-CNT	O_2-FePc-Py-G
	E_{total} (eV)	E_{total} (eV)	E_{total} (eV)	E_{total} (eV)
0	E_0 + 0.137	E_0 + 0.125	E_0 + 0.033	E_0 + 0.032
1	E_0 + 0.040	E_0 + 0.021	E_0	E_0
2	E_0	E_0	E_0 + 0.030	E_0 + 0.035
3	E_0 + 0.030	E_0 + 0.042	E_0 + 0.106	E_0 + 0.083

Finally, we obtained two main correlations (see graphical abstract) for FePc-CNT and FePc-Py-CNT when the catalytic activity where evaluated as log j_k at the constant electrode potential value of 0.8 V vs. the binding energy (M-O_2) or vs. the formal potential E_0'Fe(III)/(II), as proposed by several authors.[33,41,87,118] Both correlations agree with the previous reports[21,119,125] indicating that Py axial ligands directly affect the iron local electron density, changing the binding energy of the active site with O_2 and modulating the catalytic activity for the ORR.

4. Conclusions.

FePc-CNT and FePc-Py-CNT catalysts were investigated for ORR in both acid and basic medium, whereas the OER was studied only in alkaline media. In both media, FePc-Py-CNT electrode performed as the best catalyst compared to FePc-CNT electrode for ORR, with a potential difference ($\Delta E = E_{j10}$OER – $E_{1/2}$ORR) as bifunctional catalysts of ΔE =0.680 V, which well compares with pyrolyzed catalysts. The higher ORR and OER activity for FePc-Py-CNT vs FePc-CNT could be attributed to different factors which work synergically, as: (a) positive formal potential shift with respect to FePc-CNT due to the electron withdrawing effect of the Py axial ligand, (b) geometrical change in iron coordination hole size which modified dz^2 energy level, decreasing the strength of the Fe-O_2 interaction for the FePc-Py-CNT catalyst, and (c) the $3d_z^2$ orbital electron availability. The DFT results also indicated that the Py axial ligand modified the Fe-N distance in the FeN4 plane. Consequently, an increase of $3d_z^2$ orbital energy level simultaneously decreases the strong Fe-O_2 adduct interaction, improving the catalytic activity for ORR, in agreement with the *ex-situ* characterization of the catalyst by EPR, Mössbauer and XPS which indicate that there is a structural transformation without breaking the FePc molecule, where Py is in an axial location with respect to FePc, which generates an electron pulling character.

In the ORR, the catalyst act with the O_2 molecule with an effective rearrangement of the d_z^2 orbital, due to a change of local symmetry form of the five-coordination system to a an hexacoordinate one, decreasing the energy associated with the ORR process. On the other hand, impedance measurements indicate that this catalyst has a lower resistance to the charge transfer process, which also favours the mass transfer through the film, necessary to maintain electroneutrality in it during the ORR process.

Declaration of Competing Interest

The authors declare that they have no known competing financial interests or personal relationships that could have appeared to influence the work reported in this paper.

Acknowledgements

The authors acknowledge the funding from Fondecyt Grants 1181840, 1181037, 11170879, Conicyt/Anid PIA Proyect ACT 192175, Proyecto POSTDOC_DICYT, 022142TG_POSTDOC, Vicerrectoría de Investigación, Desarrollo e Innovación. The authors are thankful to LNLS-CNPEM (Brazil) for the project 20170843 (SXS beamline).

Author Information

Corresponding Author

Federico Tasca - *Departamento de Química de los Materiales, Facultad de Química y Biología, Universidad de Santiago de Chile, Santiago, Chile*, **ORCID iD**. https://orcid.org/0000-0002-4111-4624.

Authors

César Zúñiga Loyola - *Departamento de Química de Los Materiales, Facultad de Química y Biología, Universidad de Santiago de Chile, Santiago, Chile.* **ORCID iD**. https://orcid.org/0000-0002-0894-3383.

Gabriel Abarca - *Universidad Bernardo O'Higgins, Escuela de Obstetricia y Puericultura, Centro Integrativo de Biología y Química Aplicada (CIBQA), Santiago 8370993, Chile.* **ORCID iD**. https://orcid.org/0000-0001-8477-2275.

M.Soledad Ureta-Zañartu - *Departamento de Ciencias del Ambiente, Facultad de Química y Biología, Universidad de Santiago de Chile 14 Av. Libertador Bernardo O´Higgins 3363, Santiago, Chile.* **ORCID iD**. https://orcid.org/0000-0002-9431-9965.

Carolina Aliaga - *Departamento de Ciencias del Ambiente Facultad de Química y Biología, Universidad de Santiago de Chile, Santiago, Chile. 14 Av. Libertador Bernardo O´Higgins 3363, Santiago, Chile.* **ORCID iD**. https://orcid.org/0000-0002-1352-3164.

José H. Zagal - *Departamento de Química de los Materiales Facultad de Química y Biología, Universidad de Santiago de Chile, Santiago, Chile. 14 Av. Libertador Bernardo O´Higgins 3363, Santiago, Chile.* **ORCID iD**. https://orcid.org/0000-0002-6584-2255.

Frédéric Jaouen - *ICGM, Univ. Montpellier, CNRS, ENSCM, Montpellier, France.* **ORCID iD**. https://orcid.org/0000-0001-9836-3261.

Moulay Sougrati - *ICGM, Univ. Montpellier, CNRS, ENSCM, Montpellier, France.* **ORCID iD**. https://orcid.org/0000-0003-3740-2807.

Walter Orellana - *Departamento de Ciencias Físicas, Universidad Andrés Bello, Sazié 2212, 837-0136 Santiago, Chile.* **ORCID iD**. https://orcid.org/0000-0002-6897-3875.

References

1 Grand View Research, *Mark. Anal. Rep.*, 2020, 122.

2 S. T. Thompson, B. D. James, J. M. Huya-Kouadio, C. Houchins, D. A. DeSantis, R. Ahluwalia, A. R. Wilson, G. Kleen and D. Papageorgopoulos, *J. Power Sources*, 2018, **399**, 304–313.

3 J. K. Nørskov, J. Rossmeisl, A. Logadottir, L. Lindqvist, J. R. Kitchin, T. Bligaard and H. Jónsson, *J. Phys. Chem. B*, 2004, **108**, 17886–17892.

4 W. Zhang, W. Lai and R. Cao, *Chem. Rev.*, 2017, **117**, 3717–3797.

5 M. K. Debe, *Nature*, 2012, **486**, 43–51.

6 B. C. H. Steele and A. Heinzel, *Nature*, 2001, **414**, 345–352.

7 D. Schonvogel, J. Hülstede, P. Wagner, I. Kruusenberg, K. Tammeveski, A. Dyck, C. Agert and M. Wark, *J. Electrochem. Soc.*, 2017, **164**, F995–F1004.

8 S. Hussain, H. Erikson, N. Kongi, A. Sarapuu, J. Solla-Gullón, G. Maia, A. M. Kannan, N. Alonso-Vante and K. Tammeveski, *Int. J. Hydrogen Energy*, 2020, **45**, 31775–31797.

9 T. Reier, M. Oezaslan and P. Strasser, *ACS Catal.*, 2012, **2**, 1765–1772.

10 C. C. L. McCrory, S. Jung, J. C. Peters and T. F. Jaramillo, *J. Am. Chem. Soc.*, 2013, **135**, 16977–16987.

11 Y. Lee, J. Suntivich, K. J. May, E. E. Perry and Y. Shao-Horn, *J. Phys. Chem. Lett.*, 2012, **3**, 399–404.

12 S. Jung, C. C. L. McCrory, I. M. Ferrer, J. C. Peters and T. F. Jaramillo, *J. Mater. Chem. A*, 2016, **4**, 3068–3076.

13 P. Rüetschi and P. Delahay, *J. Chem. Phys.*, 1955, **23**, 556–560.

14 R. JASINSKI, *Nature*, 1964, **201**, 1212–1213.

15 Z. Xiang, Y. Xue, D. Cao, L. Huang, J.-F. Chen and L. Dai, *Angew. Chemie Int. Ed.*, 2014, **53**, 2433–2437.

16 G. Wu, K. L. More, C. M. Johnston and P. Zelenay, *Science (80-.).*, 2011, **332**, 443–447.

17 E. Proietti, F. Jaouen, M. Lefèvre, N. Larouche, J. Tian, J. Herranz and J.-P. Dodelet, *Nat. Commun.*, 2011, **2**, 416.

18 R. Cao, R. Thapa, H. Kim, X. Xu, M. Gyu Kim, Q. Li, N. Park, M. Liu and J. Cho, *Nat. Commun.*, 2013, **4**, 2076.

19 W. Li, A. Yu, D. C. Higgins, B. G. Llanos and Z. Chen, *J. Am. Chem. Soc.*, 2010, **132**, 17056–17058.

20 J. Yang, F. Toshimitsu, Z. Yang, T. Fujigaya and N. Nakashima, *J. Mater. Chem. A*, 2017, **5**, 1184–1191.

21 G. Abarca, M. Viera, C. Aliaga, J. F. Marco, W. Orellana, J. H. Zagal and F. Tasca, *J. Mater. Chem. A*, 2019, **7**, 24776–24783.

22 L. Wu, Q. Li, C. H. Wu, H. Zhu, A. Mendoza-Garcia, B. Shen, J. Guo and S. Sun, *J. Am. Chem. Soc.*, 2015, **137**, 7071–7074.

23 X. Lu and C. Zhao, *J. Mater. Chem. A*, 2013, **1**, 12053–12059.

24 L. Han, S. Dong and E. Wang, *Adv. Mater.*, 2016, **28**, 9266–9291.

25 F. Yu, H. Zhou, Y. Huang, J. Sun, F. Qin, J. Bao, W. A. Goddard, S. Chen and Z. Ren, *Nat. Commun.*, 2018, **9**, 1–9.

26 A. Sarapuu, E. Kibena-Põldsepp, M. Borghei and K. Tammeveski, *J. Mater. Chem. A*, 2018, **6**,

776–804.

27 F. Jaouen, J. Herranz, M. Lefévre, J. P. Dodelet, U. I. Kramm, I. Herrmann, P. Bogdanoff, J. Maruyama, T. Nagaoka, A. Garsuch, J. R. Dahn, T. Olson, S. Pylypenko, P. Atanassov and E. A. Ustinov, *ACS Appl. Mater. Interfaces*, 2009, **1**, 1623–1639.

28 N. D. Leonard, S. Wagner, F. Luo, J. Steinberg, W. Ju, N. Weidler, H. Wang, U. I. Kramm and P. Strasser, *ACS Catal.*, 2018, **8**, 1640–1647.

29 N. Zion, D. A. Cullen, P. Zelenay and L. Elbaz, *Angew. Chemie - Int. Ed.*, 2020, **59**, 2483–2489.

30 R. Praats, M. Käärik, A. Kikas, V. Kisand, J. Aruväli, P. Paiste, M. Merisalu, J. Leis, V. Sammelselg, J. H. Zagal, S. Holdcroft, N. Nakashima and K. Tammeveski, *Electrochim. Acta*, , DOI:10.1016/j.electacta.2019.135575.

31 Y. Kumar, E. Kibena-Põldsepp, J. Kozlova, M. Rähn, A. Treshchalov, A. Kikas, V. Kisand, J. Aruväli, A. Tamm, J. C. Douglin, S. J. Folkman, I. Gelmetti, F. A. Garcés-Pineda, J. R. Galán-Mascarós, D. R. Dekel and K. Tammeveski, *ACS Appl. Mater. Interfaces*, , DOI:10.1021/acsami.1c06737.

32 N. Zion, A. Friedman, N. Levy and L. Elbaz, *Adv. Mater.*, 2018, **30**, 1–6.

33 J. H. Zagal and M. T. M. Koper, *Angew. Chemie Int. Ed.*, 2016, **55**, 14510–14521.

34 C. Zúñiga, C. Candia-Onfray, R. Venegas, K. Muñoz, J. Urra, M. Sánchez-Arenillas, J. F. Marco, J. H. Zagal and F. J. Recio, *Electrochem. commun.*, 2019, **102**, 78–82.

35 S. Pylypenko, S. Mukherjee, T. S. Olson and P. Atanassov, *Electrochim. Acta*, 2008, **53**, 7875–7883.

36 M. Kobayashi, H. Niwa, M. Saito, Y. Harada, M. Oshima, H. Ofuchi, K. Terakura, T. Ikeda, Y. Koshigoe, J. I. Ozaki and S. Miyata, *Electrochim. Acta*, 2012, **74**, 254–259.

37 R. Praats, I. Kruusenberg, M. Käärik, U. Joost, J. Aruväli, P. Paiste, R. Saar, P. Rauwel, M. Kook, J. Leis, J. H. Zagal and K. Tammeveski, *Electrochim. Acta*, 2019, **299**, 999–1010.

38 M. Mooste, T. Tkesheliadze, J. Kozlova, A. Kikas, V. Kisand, A. Treshchalov, A. Tamm, J. Aruväli, J. H. Zagal, A. M. Kannan and K. Tammeveski, *Int. J. Hydrogen Energy*, 2021, **46**, 4365–4377.

39 F. Jaouen, A. M. Serventi, M. Lefèvre, J.-P. Dodelet and P. Bertrand, *J. Phys. Chem. C*, 2007, **111**, 5971–5976.

40 U. I. Kramm, J. Herranz, N. Larouche, T. M. Arruda, M. Lefèvre, F. Jaouen, P. Bogdanoff, S. Fiechter, I. Abs-Wurmbach, S. Mukerjee and J.-P. Dodelet, *Phys. Chem. Chem. Phys.*, 2012, **14**, 11673–11688.

41 R. Venegas, F. J. Recio, C. Zuñiga, M. Viera, M.-P. Oyarzún, N. Silva, K. Neira, J. F. Marco, J. H. Zagal and F. Tasca, *Phys. Chem. Chem. Phys.*, 2017, **19**, 20441–20450.

42 J.-P. Randin, *Electrochim. Acta*, 1974, **19**, 83–85.

43 F. Beck, *J. Appl. Electrochem.*, 1977, **7**, 239–245.

44 J. P. Collman, R. Boulatov, C. J. Sunderland and L. Fu, *Chem. Rev.*, 2004, **104**, 561–588.

45 S. Yoshikawa and A. Shimada, *Chem. Rev.*, 2015, **115**, 1936–1989.

46 S. Hematian, I. Garcia-Bosch and K. D. Karlin, *Acc. Chem. Res.*, 2015, **48**, 2462–2474.

47 S. Herrera, F. Tasca, F. J. Williams, E. J. Calvo, P. Carro and R. C. Salvarezza, *Langmuir*, 2017, **33**, 9565–9572.

48 J. Govan, W. Orellana, J. H. Zagal and F. Tasca, *J. Solid State Electrochem.*, 2021, **25**, 15–31.

49 M. Viera, J. Riquelme, C. Aliaga, J. F. Marco, W. Orellana, J. H. Zagal and F. Tasca, *Front.*

Chem., 2020, **8**, 1–12.

50 R. Venegas, F. J. Recio, J. Riquelme, K. Neira, J. F. Marco, I. Ponce, J. H. Zagal and F. Tasca, *J. Mater. Chem. A*, 2017, **5**, 12054–12059.

51 R. Z. Snitkoff, N. Levy, I. Ozery, S. Ruthstein and L. Elbaz, *Carbon N. Y.*, 2019, **143**, 223–229.

52 L. Elbaz, E. Korin, L. Soifer and A. Bettelheim, *J. Electrochem. Soc.*, 2010, **157**, B27.

53 L. Elbaz, E. Korin, L. Soifer and A. Bettelheim, *J. Phys. Chem. Lett.*, 2010, **1**, 398–401.

54 N. Alzate-Carvajal, L. M. Bolivar-Pineda, V. Meza-Laguna, V. A. Basiuk, E. V. Basiuk and E. A. Baranova, *ChemElectroChem*, 2020, **7**, 428–436.

55 A. Abbaspour and E. Mirahmadi, *Electrochim. Acta*, 2013, **105**, 92–98.

56 L. Xu, H. Lei, Z. Zhang, Z. Yao, J. Li, Z. Yu and R. Cao, *Phys. Chem. Chem. Phys.*, 2017, **19**, 9755–9761.

57 J. Yang, J. Tao, T. Isomura, H. Yanagi, I. Moriguchi and N. Nakashima, *Carbon N. Y.*, 2019, **145**, 565–571.

58 J. L. Kneebone, S. L. Daifuku, J. A. Kehl, G. Wu, H. T. Chung, M. Y. Hu, E. E. Alp, K. L. More, P. Zelenay, E. F. Holby and M. L. Neidig, *J. Phys. Chem. C*, 2017, **121**, 16283–16290.

59 U. I. Kramm, L. Ni and S. Wagner, *Adv. Mater.*, 2019, **31**, 1805623.

60 F. Tasca, W. Harreither, R. Ludwig, J. J. Gooding and L. Gorton, *Anal. Chem.*, 2011, **83**, 3042–3049.

61 X. Chen, N. Wang, K. Shen, Y. Xie, Y. Tan and Y. Li, *ACS Appl. Mater. Interfaces*, 2019, **11**, 25976–25985.

62 R. Burkitt, T. R. Whiffen and E. H. Yu, *Appl. Catal. B Environ.*, 2016, **181**, 279–288.

63 A. J. Bard and L. R. Faulkner, *Electrochemical Method. Fundamentals and Applications*, JOHN WILEY & SONS, INC, 2º., 2001.

64 R. E. Davis, G. L. Horvath and C. W. Tobias, *Electrochim. Acta*, 1967, **12**, 287–297.

65 K. S. L. David Reynolds Lide, *CRC Handbook of Chemistry and Physics*, 82nd edn., 2001.

66 C. Wei, S. Sun, D. Mandler, X. Wang, S. Z. Qiao and Z. J. Xu, *Chem. Soc. Rev.*, 2019, **48**, 2518–2534.

67 F. Fernández, C. Berríos, E. Garrido-Ramírez, N. Escalona, C. Gutiérrez and M. S. Ureta-Zañartu, *J. Appl. Electrochem.*, 2014, **44**, 1295–1306.

68 N. E. and E. Gileadi, *Review: Physical Electrochemistry – Fundamentals, Techniques, and Applications*, WILEY-VCH, Germany, Second Edi., 2019.

69 S. Trasatti and O. A. Petrii, *Pure Appl. Chem.*, 1991, **63**, 711–734.

70 G. Gro, *PC-Mos II Version 1.0 Manual and Program Documentation*, Germany, 1993.

71 A. Pizarro, G. Abarca, C. Gutiérrez-Cerón, D. Cortés-Arriagada, F. Bernardi, C. Berrios, J. F. Silva, M. C. Rezende, J. H. Zagal, R. Oñate and I. Ponce, *ACS Catal.*, 2018, **8**, 8406–8419.

72 M. C. Biesinger, B. P. Payne, A. P. Grosvenor, L. W. M. Lau, A. R. Gerson and R. S. C. Smart, *Appl. Surf. Sci.*, 2011, **257**, 2717–2730.

73 G. Kresse and J. Furthmüller, *Phys. Rev. B*, 1996, **54**, 11169–11186.

74 J. P. Perdew, K. Burke and M. Ernzerhof, *Phys. Rev. Lett.*, 1997, **78**, 1396–1396.

75 S. Grimme, *J. Comput. Chem.*, 2006, **27**, 1787–1799.

76 P. E. Blöchl, *Phys. Rev. B*, 1994, **50**, 17953–17979.

77 C. Aliaga, P. Torres and F. Silva, *Magn. Reson. Chem.*, 2012, **50**, 779–783.

78 B. Corzilius, K. P. Dinse and K. Hata, *Phys. Chem. Chem. Phys.*, 2007, **9**, 6063–6072.

79 S. S. Rao, A. Stesmans, J. V. Noyen, P. Jacobs and B. Sels, *J. Phys. Condens. Matter*, 2011, **23**, 455801.

80 A. MacCragh, C. B. Storm and W. S. Koski, *J. Am. Chem. Soc.*, 1965, **87**, 1470–1476.

81 G. V Oubdraogo, C. More, Y. Richard and D. Benlian, *Inorg. Chem.*, 1981, **20**, 4387–4393.

82 D. A. Scherson, C. A. Fierro, D. Tryk, S. L. Gupta, E. B. Yeager, J. Eldridge and R. W. Hoffman, *J. Electroanal. Chem. Interfacial Electrochem.*, 1985, **184**, 419–426.

83 D. A. Scherson, S. B. Yao, E. B. Yeager, J. Eldridge, M. E. Kordesch and R. W. Hoffman, *J. Phys. Chem.*, 1983, **87**, 932–943.

84 C. Cao, S. Dahal, M. Shang, A. M. Beatty, W. Hibbs, C. E. Schulz and W. R. Scheidt, *Inorg. Chem.*, 2003, **42**, 5202–5210.

85 W. Cheng, P. Yuan, Z. Lv, Y. Guo, Y. Qiao, X. Xue, X. Liu, W. Bai, K. Wang, Q. Xu and J. Zhang, *Appl. Catal. B Environ.*, 2020, **260**, 118198.

86 E. Kuzmann, Z. Homonnay, A. Vértes, S. Li, H. Yin, Y. Wei, A. Nath, X. Chen and J. Li, *J. Solid State Chem.*, 2003, **170**, 118–123.

87 J. H. Zagal, S. Griveau, J. F. Silva, T. Nyokong and F. Bedioui, *Coord. Chem. Rev.*, 2010, **254**, 2755–2791.

88 E. Erasmus, *J. Electron Spectros. Relat. Phenomena*, 2018, **223**, 84–88.

89 S. Pal, in *Pyridine*, ed. IntechOpen, InTech, 1er edn., 2018.

90 D. K. Lavallee, M. D. Baughman and M. P. Phillips, *J. Am. Chem. Soc.*, 1977, **99**, 718–724.

91 M.-S. Liao and S. Scheiner, *J. Chem. Phys.*, 2002, **116**, 3635–3645.

92 J. H. Zagal, S. Griveau, M. Santander-Nelli, S. G. Granados and F. Bedioui, *J. Porphyr. Phthalocyanines*, 2012, **16**, 713–740.

93 Y. Liu, X. Yue, K. Li, J. Qiao, D. P. Wilkinson and J. Zhang, *Coord. Chem. Rev.*, 2016, **315**, 153–177.

94 M. Rauf, Y. Di Zhao, Y. C. Wang, Y. P. Zheng, C. Chen, X. D. Yang, Z. Y. Zhou and S. G. Sun, *Electrochem. commun.*, 2016, **73**, 71–74.

95 A. A. Gewirth and M. S. Thorum, *Inorg. Chem.*, 2010, **49**, 3557–3566.

96 M. F. Labata, G. Li, J. Ocon and P. Y. A. Chuang, *J. Power Sources*, 2021, **487**, 229356.

97 J. D. Yi, R. Xu, Q. Wu, T. Zhang, K. T. Zang, J. Luo, Y. L. Liang, Y. B. Huang and R. Cao, *ACS Energy Lett.*, 2018, **3**, 883–889.

98 N. Ramaswamy, U. Tylus, Q. Jia and S. Mukerjee, *J. Am. Chem. Soc.*, 2013, **135**, 15443–15449.

99 N. Ramaswamy and S. Mukerjee, *Adv. Phys. Chem.*, 2012, **2012**, 1–17.

100 U. Tylus, Q. Jia, K. Strickland, N. Ramaswamy, A. Serov, P. Atanassov and S. Mukerjee, *J. Phys. Chem. C*, 2014, **118**, 8999–9008.

101 J. Zagal, M. Páez, A. A. Tanaka, J. R. dos Santos and C. A. Linkous, *J. Electroanal. Chem.*, 1992, **339**, 13–30.

102 J. H. Zagal and F. Bedioui., *Electrochemistry of N4 Macrocyclic Metal Complexes*, Springer Science., Switzerland, Second Edi., 2016, vol. 1.

103 I. Ponce, J. F. Silva, R. Oñate, M. C. Rezende, M. A. Páez, J. Pavez and J. H. Zagal, *Electrochem. commun.*, 2011, **13**, 1182–1185.

104 K. Chen, K. Liu, P. An, H. Li, Y. Lin, J. Hu, C. Jia, J. Fu, H. Li, H. Liu, Z. Lin, W. Li, J. Li, Y.-R.

Lu, T.-S. Chan, N. Zhang and M. Liu, *Nat. Commun.*, 2020, **11**, 4173.

105 J. Han, X. Meng, L. Lu, J. Bian, Z. Li and C. Sun, *Adv. Funct. Mater.*, 2019, **29**, 1808872.

106 X. Yang, K. Li, J. Lv, X. Chen, H. Y. Zang, H. Q. Tan, Y. H. Wang and Y. G. Li, *ChemElectroChem*, 2018, **5**, 3279–3286.

107 Q. Liu, Y. Wang, L. Dai and J. Yao, *Adv. Mater.*, 2016, **28**, 3000–3006.

108 R. M. Yadav, J. Wu, R. Kochandra, L. Ma, C. S. Tiwary, L. Ge, G. Ye, R. Vajtai, J. Lou and P. M. Ajayan, *ACS Appl. Mater. Interfaces*, 2015, **7**, 11991–12000.

109 N. Chebotareva and T. Nyokong, *Electrochim. Acta*, 1997, **42**, 3519–3524.

110 M. Bajdich, M. García-Mota, A. Vojvodic, J. K. Nørskov and A. T. Bell, *J. Am. Chem. Soc.*, 2013, **135**, 13521–13530.

111 J. Greeley and N. M. Markovic, *Energy Environ. Sci.*, 2012, **5**, 9246–9256.

112 W. Wan, C. A. Triana, J. Lan, J. Li, C. S. Allen, Y. Zhao, M. Iannuzzi and G. R. Patzke, *ACS Nano*, 2020, **14**, 13279–13293.

113 Y. Cheng, X. Wu, J. P. Veder, L. Thomsen, S. P. Jiang and S. Wang, *Energy Environ. Mater.*, 2019, **2**, 5–17.

114 S. Chen, J. Duan, M. Jaroniec and S. Z. Qiao, *Angew. Chemie - Int. Ed.*, 2013, **52**, 13567–13570.

115 R. Akram, M. A. Ud Din, S. U. Dar, A. Arshad, W. Liu, Z. Wu and D. Wu, *Nanoscale*, 2018, **10**, 5658–5666.

116 L. Wei, L. Qiu, Y. Liu, J. Zhang, D. Yuan and L. Wang, *ACS Sustain. Chem. Eng.*, 2019, **7**, 14180–14188.

117 S. Neya, *Molecules*, 2013, **18**, 3168–3182.

118 J. H. Zagal, F. Javier Recio, C. A. Gutierrez, C. Zuñiga, M. A. Páez and C. A. Caro, *Electrochem. commun.*, 2014, **41**, 24–26.

119 J. Riquelme, K. Neira, J. F. Marco, P. Hermosilla-Ibáñez, W. Orellana, J. H. Zagal and F. Tasca, *Electrochim. Acta*, 2018, **265**, 547–555.

Figures

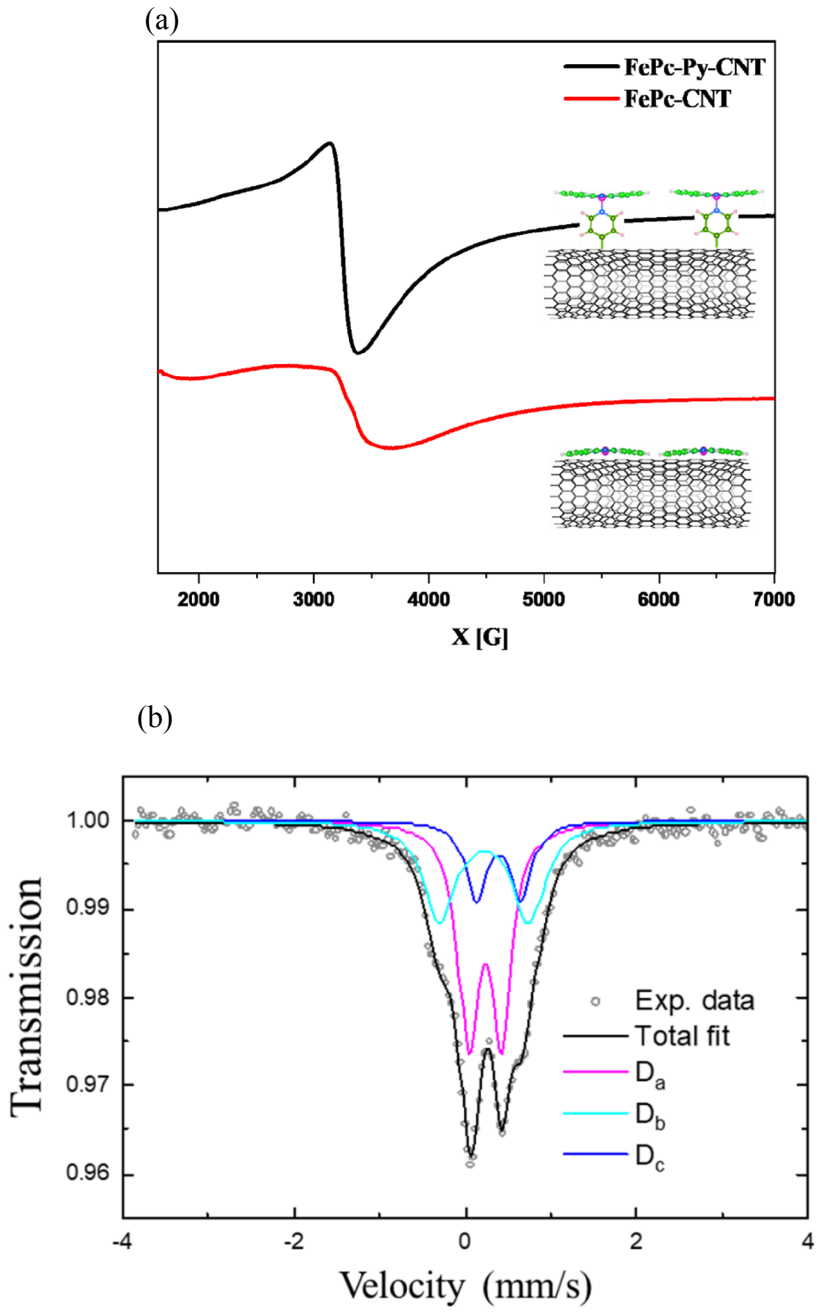

Figure 1. (a) EPR spectra for FePc-Py-CNT and FePC-CNT at 298K. (b) Mössbauer spectra determined for the FePc-Py-CNT catalyst at 295K.

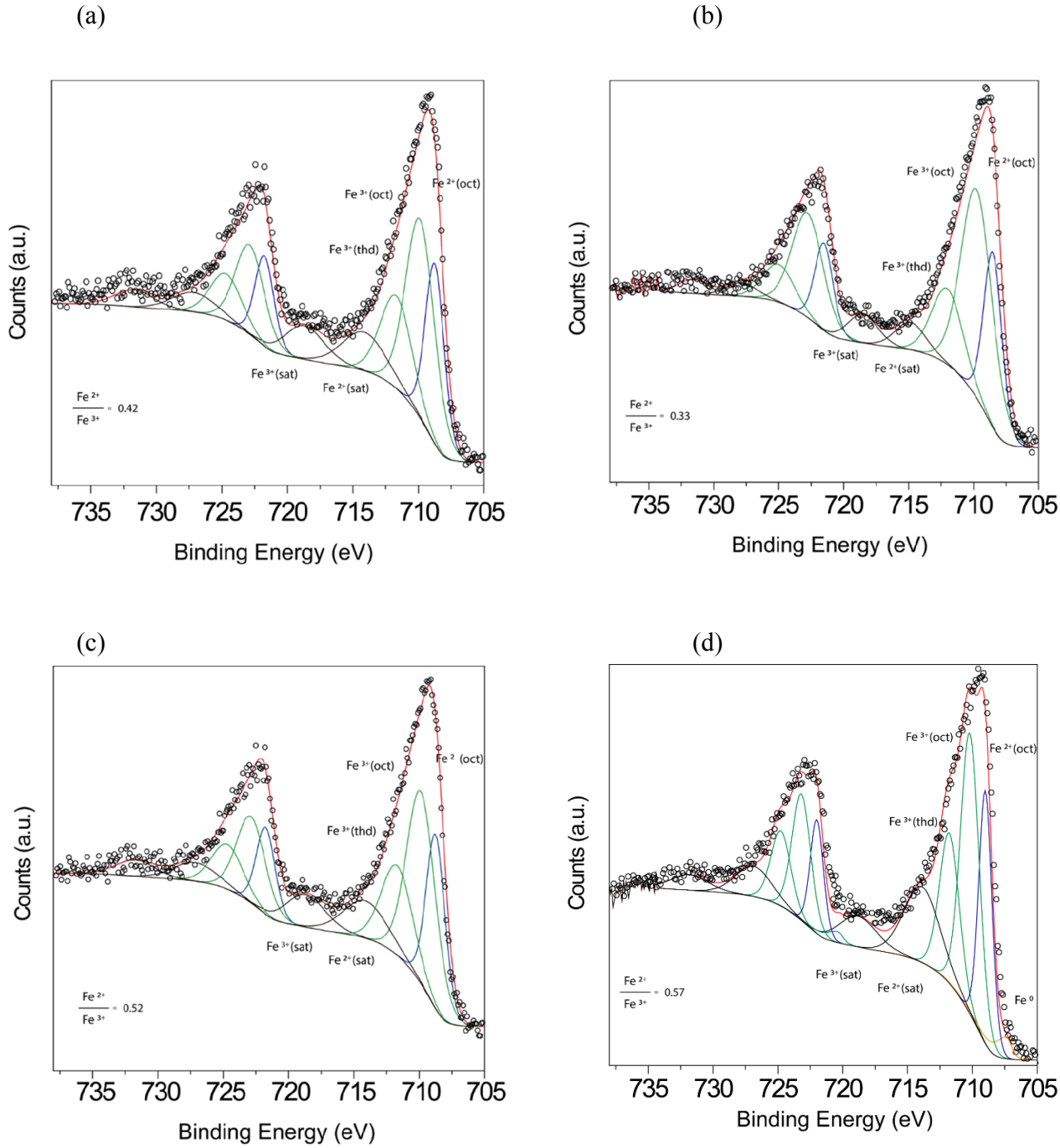

Figure 2. XPS spectrum for (a, c) FePc-CNT, (b, d) FePc-Py-CNT, (a, b) before, and (c, d) after exposition to O_2.

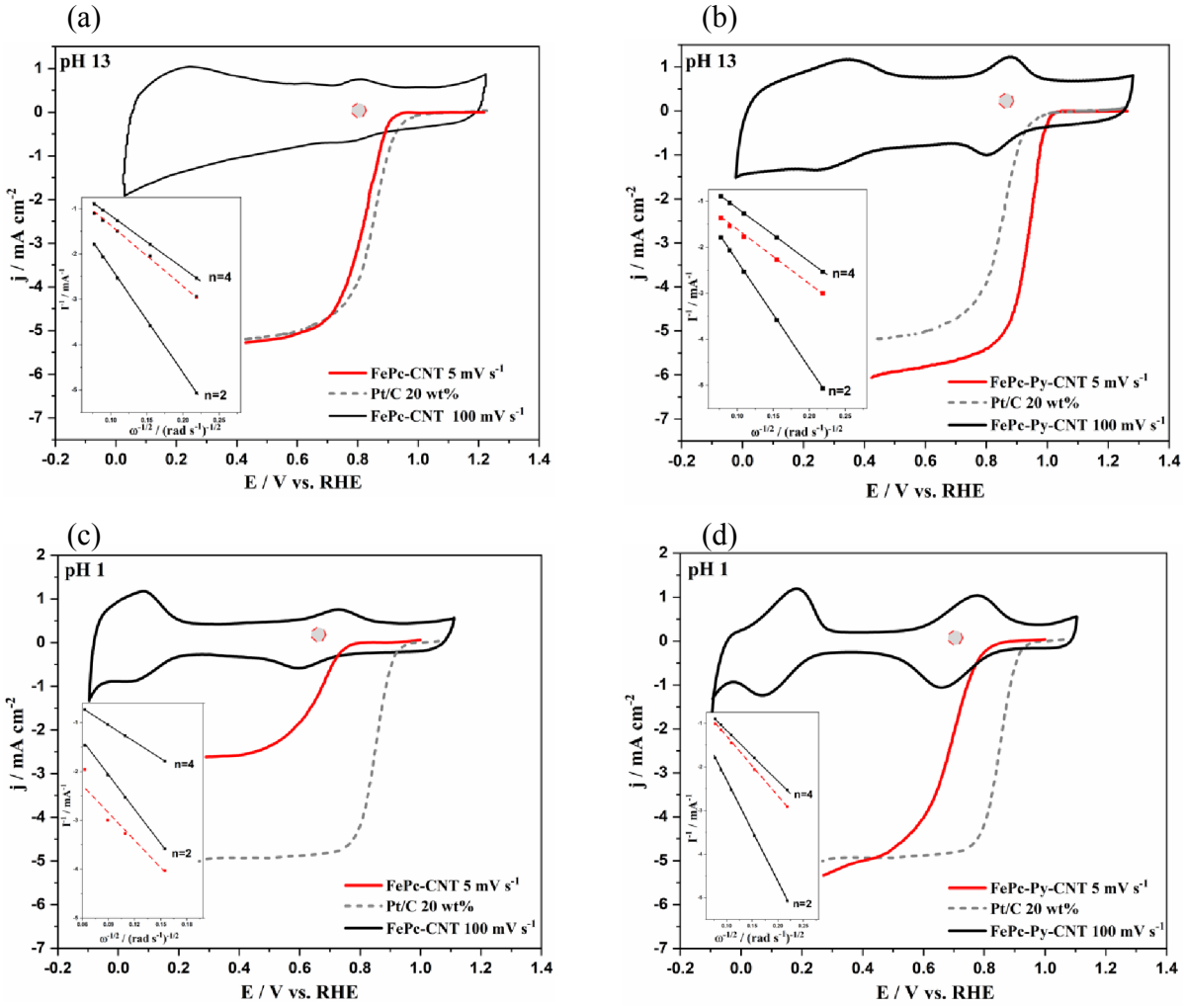

Figure 3. Cyclic Voltammetry at 100mV s^{-1} in N_2 and polarization curve at 5mV s^{-1}, 1600 rpm and O_2 saturated solution for (a, c) FePc-CNT, (b, d) FePc-Py-CNT, and (a-d) Pt/C 20wt% in (a, b) 0.1M KOH and (c, d) 0.1M H_2SO_4 solution. (a-b) Inset show Koutecky-Levich plot determined at 0.35 and 0.45 V vs. RHE in acid and alkaline media, respectively.

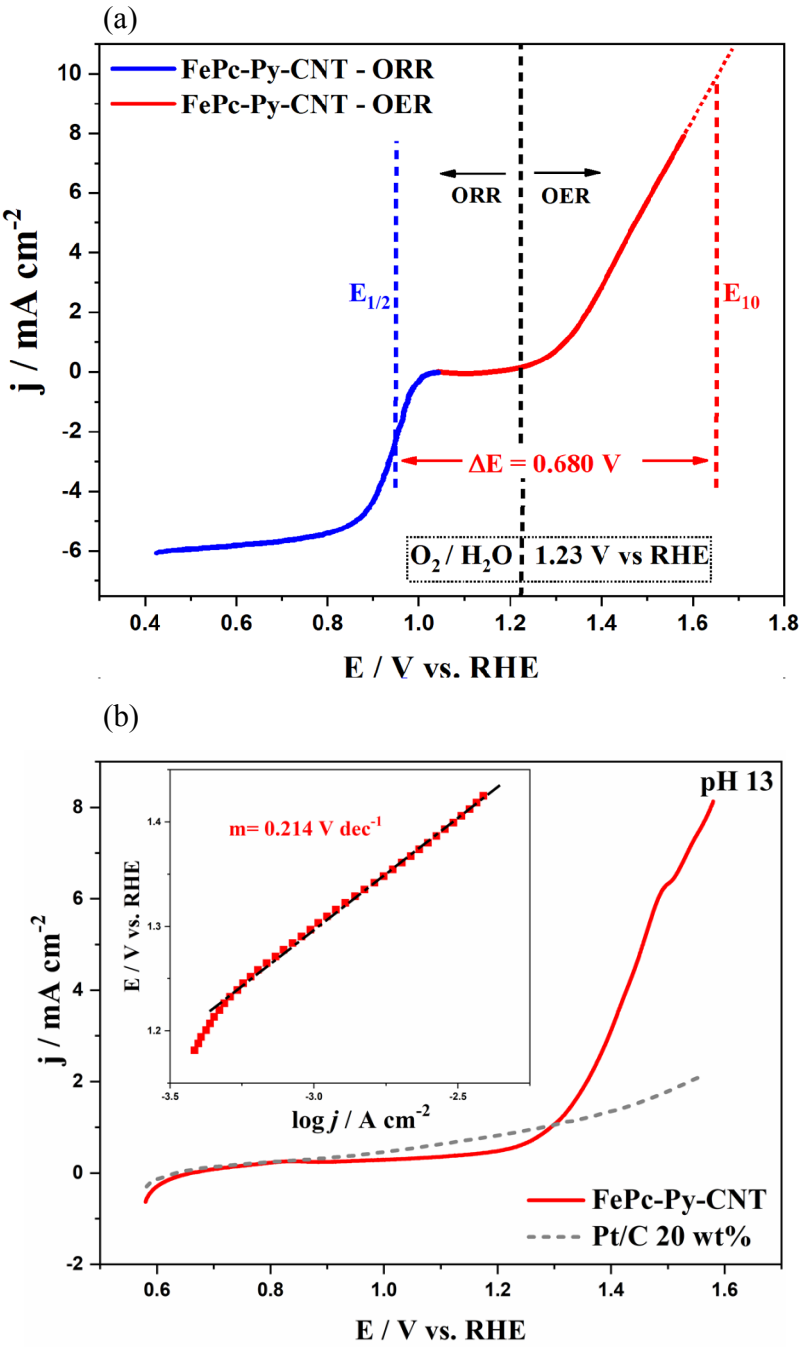

Figure 4. (a) Polarisation curves at 5 mv s^{-1} for ORR and OER in 0.1M KOH with FePc-Py-CNT catalyst. (b) polarisation curve at 5 mV s^{-1} in deaerated 0.1M KOH solution and inset with Tafel plot for OER.

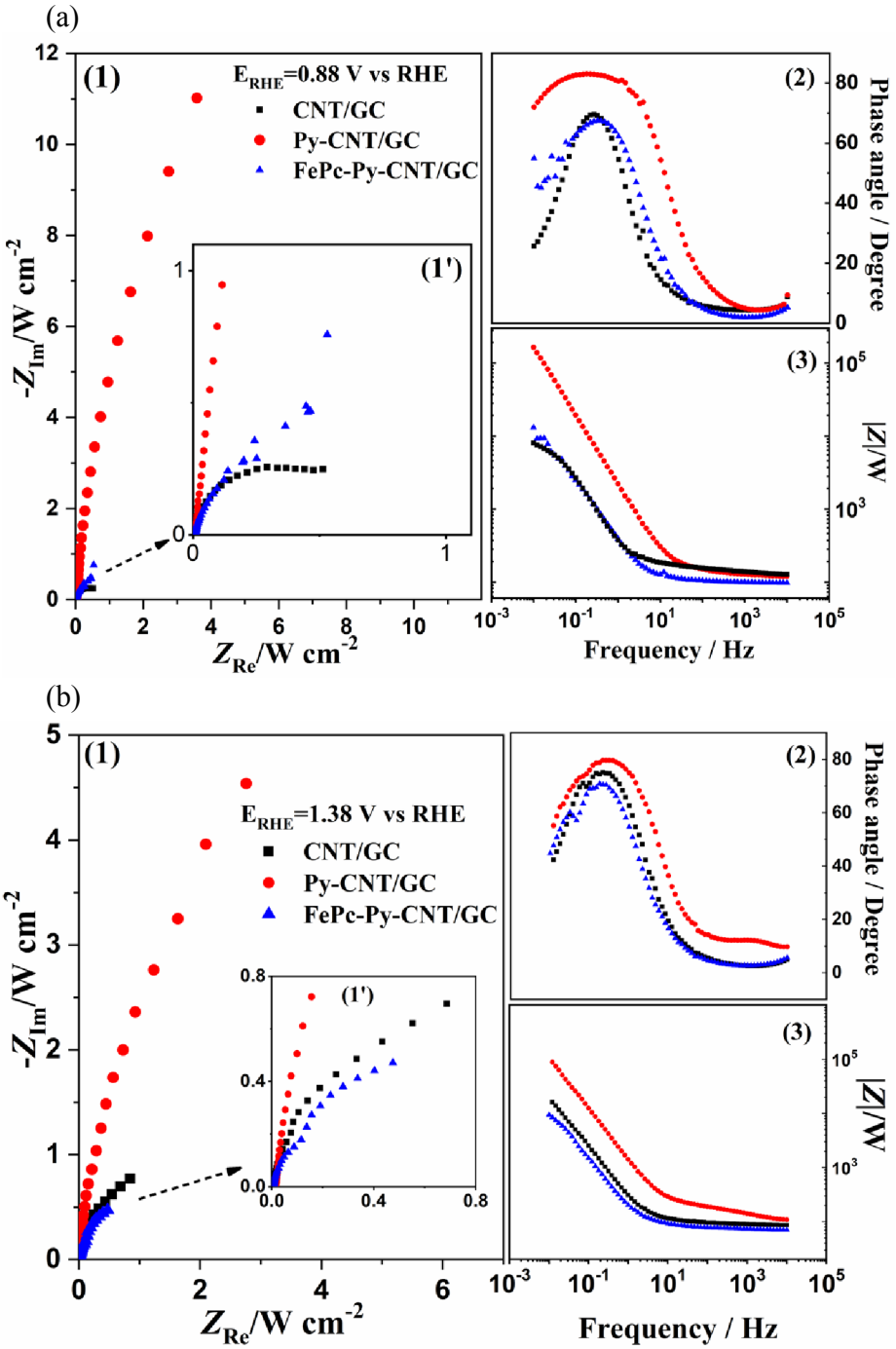

Figure 5. (**a**-1) Nyquist plots at 0.88 V vs. RHE, (**a**-2, a-3) Bode plots for CNT/GC, Py-CNT/GC and FePc-Py-CNT/GC under N_2 and O_2 atmosphere in 0.1M KOH for ORR. (**b**-1) Nyquist plots at 1.38 V vs. RHE, (**b**-2, b-3) Bode plots for CNT/GC, Py-CNT/GC and FePc-Py-CNT/GC under N_2 and O_2 atmosphere in 0.1M KOH for OER.

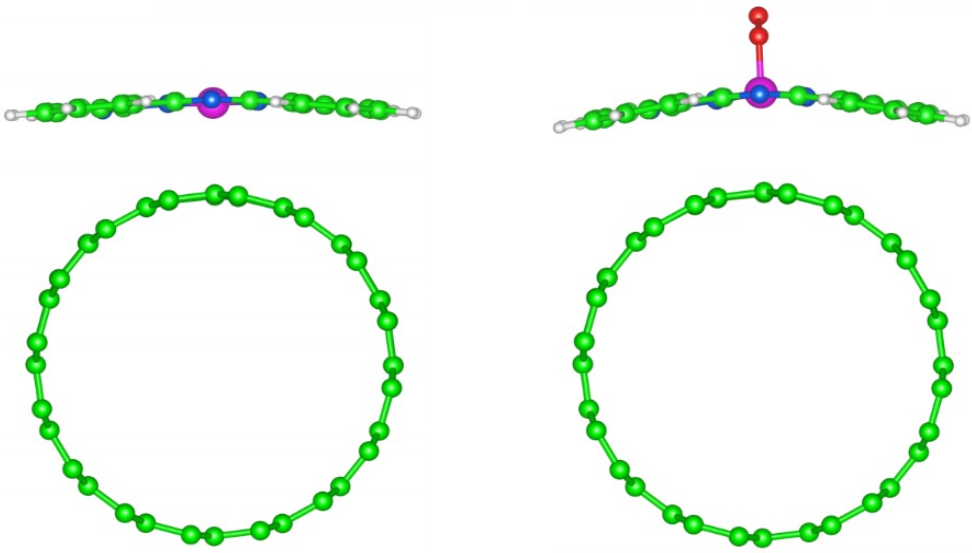

Figure 6. Image of calculated formation of FePc-CNT directly bound to a Carbon Nanotube, with blue, purple, red, and green colour for nitrogen, iron, oxygen, and carbon atoms respectively.

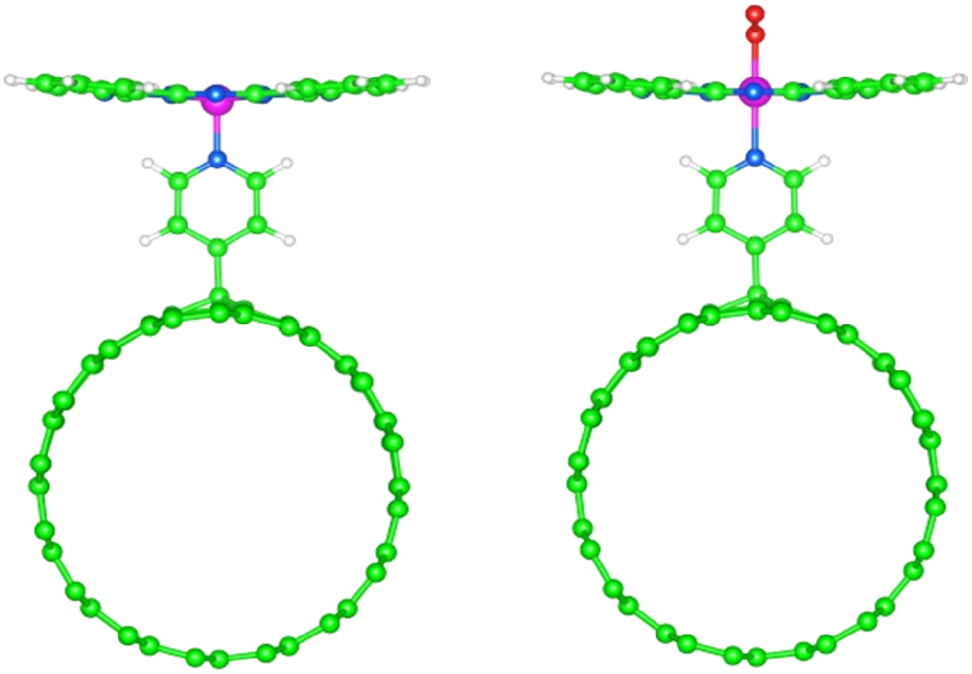

Figure 7: Computed structure of FePc bound to carbon nanotubes through amino pyridine linkages, with and without the presence of molecular oxygen, and using blue, purple, red, and green colour for nitrogen, iron, oxygen, and carbon atoms respectively.